Lead-field Bases for Electroencephalography Source Imaging

David Weinstein, Leonid Zhukov, and Chris Johnson

Scientific Computing and Imaging Institute
School of Computing
University of Utah

Abstract

In recent years, significant progress has been made in the area of electroencephalography (EEG) source imaging. Source localization on simple spherical models has become increasingly efficient, with consistently reported accuracy of within 5 mm. In contrast, source localization on realistic head models remains slow, with subcentimeter accuracy being the exception rather than the norm. A primary reason for this discrepancy is that most source imaging techniques are based on lead fields. While the lead field for simplified geometries can be easily computed analytically, an efficient method for computing realistic domain lead fields has, until now, remained elusive. In this paper, we propose two efficient methods for computing realistic EEG lead-field bases: the first is element oriented, and the second is node oriented. We compare these two bases, discuss how they can be used to apply recent source imaging methods to realistic models, and report timings for constructing the bases.

Keywords: Inverse EEG, Source localization, Finite element method, Lead field, Reciprocity

Introduction

Neural processes, such as perception, coordination, cognition, are carried out via the propagation of electrical impulses through the brain. These impulses give rise to electromagnetic fields that can be measured extracranially by sensitive recording devices. The measurement of electric potentials over time is referred to as electroencephalography (EEG), and the measurement of magnetic signals as magnetoencephalography (MEG). The practice through which we infer the inter-cranial sources that give rise to these measurements is termed the *neural source imaging* problem. Neural source imaging is a fundamental problem in neuroscience. Learning precisely which regions of the brain are active at a particular time is a central problem in fields ranging from cognitive science to neuropathology to surgical planning.

The distribution of an electromagnetic field in the head is described by the linear Poisson equation

$$\nabla \cdot (\sigma \nabla \phi) = \nabla \cdot \mathbf{J}^{\mathbf{s}}, \quad \text{in} \ \ \Omega \tag{1}$$

with no-flux Neumann boundary conditions on the scalp

$$\sigma (\nabla \phi) \cdot \mathbf{n} = 0, \quad \text{on} \ \ \Gamma_\Omega, \tag{2}$$

Address correspondence to Chris Johnson, Scientific Computing and Imaging Institute, School of Computing, University of Utah, Salt Lake City, UT 84112. Electronic mail: crj@cs.utah.edu; David Weinstein, electronic mail: dmw@cs.utah.edu; Leonid Zhukov, electronic mail: zhukov@cs.utah.edu

where σ is the electrical conductivity tensor, ϕ is the electric potential, and $\mathbf{J}^{\mathbf{s}}$ are the electric current sources. From the linearity of (1), it follows that the mapping from electric sources within the cranium to scalp recordings on the outside of the scalp can be represented by a linear operator $\mathbf{L}$. Given a particular configuration of sources, $\mathbf{s}$, the resultant recordings, ϕ_r, and the noise in the system, $\mathbf{n}$, we represent this relation as $\phi_r = \mathbf{Ls} + \mathbf{n}$. $\mathbf{L}$ is the so-called *lead-field matrix*[1] and contains information about the geometry and conductivity of the model.

The problem of interest in source imaging is this: given a set of recordings, ϕ_r, knowing $\mathbf{L}$, and making certain assumptions about $\mathbf{n}$, determine $\mathbf{s}$, the set of sources that gave rise to those recordings. The solution to this problem consists of two steps: building the lead-field matrix $\mathbf{L}$, and "inverting" it. Finding the inverse of $\mathbf{L}$ is an ill-posed problem and its solution requires regularization. There exist many different regularization methods, as well as many papers describing their application to EEG/MEG.[3, 14, 17] All of them assume that $\mathbf{L}$ either is known *a priori* or can be easily constructed. While it is true that $\mathbf{L}$ is easy to construct for simple geometries like spheres (or in other cases where an analytic solution to the forward problem exists), building the $\mathbf{L}$ matrix is much more complicated for geometries based on real patient data.

In this paper, we will concentrate on the construction of the $\mathbf{L}$ matrix. We propose two efficient methods for building $\mathbf{L}$ for realistic EEG models with realistic geometries as well as inhomogeneous and anisotropic conductivities.

Background

The lead-field matrix, $\mathbf{L}$, defines a projection from current sources at discrete locations in the cranium to potential measurements at discrete recording sites on the scalp. That is, entry $\mathbf{L_{ij}}$ corresponds to the potential that would be measured at recording site ϕ_i due specifically to source $\mathbf{s_j}$. Sources are traditionally defined by three orthogonal dipoles, $\mathbf{s_{jx}}, \mathbf{s_{jy}}, \mathbf{s_{jz}}$ and source positions are generally located on a regular grid of hexahedral cells covering the domain of interest.

In a number of application papers, researchers have been able to compute the $\mathbf{L}$ basis by exploiting analytic equations for each entry in $\mathbf{L}$. The equations for the matrix entries, or *kernels*, for each method can be found in Mosher's review of forward and inverse EEG and MEG methods.[13] For most of them, the $\mathbf{L}$ matrix is constructed one element at a time by evaluating the analytic expression for the potential at each recordings site (the rows), due to a source at each location in the domain (the columns).

While fast analytic expressions exist for the potentials in spherical models, these solutions cannot be applied to realistic head models. Rather, a complete forward numerical solution must be computed in order to determine the elec-

trode potentials due to each source. These realistic model forward solutions can be generated using the boundary element method or finite element method (FEM).[7, 6, 12] Both methods can faithfully represent the complex boundaries and inhomogeneous regions of realistic models. The FEM has the additional advantage that it can capture anisotropic conductivities of the domain. For these reasons, we have chosen to use the FEM for our lead-field calculations.

The main idea behind the FEM is to reduce a continuous problem with infinitely many unknown field values to a finite number of unknowns by discretizing the solution region into elements. The value at any point in the field can then be approximated by interpolation functions within the elements. These interpolation functions are specified in terms of the field values at the corners of the elements, points known as nodes. We note that for linearly interpolation potentials, the electric field is constant within an element.

Given a geometric model, the FEM proceeds by assembling the matrix equations to build the stiffness matrix $\mathbf{A}$. This can be done using, for example, a Rayleigh-Ritz or Galerkin method.[5] Boundary conditions are then imposed and source currents are applied. These boundary and source conditions are incorporated within the right hand side of the system (vector $\mathbf{b}$). Details of the FEM method can be found in Refs. [5, 6, 12, 21]. Application of the FEM reduces Poisson's equation to the linear system

$$\mathbf{A}_{ij}\phi_j = \mathbf{b}_i \qquad (3)$$

where ϕ are the unknown potentials at the nodes of the volume.

When we use a realistic FEM model (3 mm resolution), and the described forward numerical construction, we may require upwards of a minute of processor time on modern architectures (e.g., an SGI MIPS R10000 processor) to solve a forward simulation. Because of this computational expense, it seems feasible to build a lead field for only a very sparse grid of sources. Even a 16^3 grid (12 mm resolution), for example, with three orthogonal dipole components per cell, would require over a day of continuous computation to build $\mathbf{L}$.

Methods

We now introduce two novel methods for constructing the lead-field matrix $\mathbf{L}$. Using these methods, we are enable to construct $\mathbf{L}$ matrices for a head model with 3 mm cell resolution (64^3 grid) in under 10 min.

Element Basis

As discussed earlier, the traditional method of constructing the $\mathbf{L}$ matrix is to place three orthogonal sources in each cell of a volume domain, and for each dipole source, compute the voltages at the electrodes. For a volume mesh consisting of N tetrahedral elements, this requires computing ($N \times 3$) forward solutions.

In constructing the $\mathbf{L}$ matrix, we would like to achieve the maximal possible resolution of sources for our model: one dipole per tetrahedral element. We would also like to take advantage of the fact that when using the FEM, we compute the potentials not only on the surfaces (as in the boundary element method), but through the entire volume. We can achieve both goals using the *principle of reciprocity*.

The reciprocity principle was introduced into the biophysical domain by Helmholtz[4] and was applied to the problem of electrocardiography by McFee and Johnston.[10] It was further developed by Plonsey,[18] and was subsequently adapted to the EEG problem by Rush and Driscoll in 1969,[19] when they proved the applicability of reciprocity to anisotropic conductors. The reciprocity principle states that given a dipole (an equivalent source), $\mathbf{p}$, and a need to know the resulting potential difference between two points A and B, it is sufficient to know the electric field $\mathbf{E}$ at the dipole location resulting from a current, I, placed between points A and B:

$$\frac{(\mathbf{E} \cdot \mathbf{p})}{-I} = \phi_{\mathbf{A}} - \phi_{\mathbf{B}}. \qquad (4)$$

So, rather than iteratively placing a source in every element and computing a forward solution at the electrodes, we can "invert" this process: we place a source and sink at pairs of electrodes, and for each pair compute the resulting electric field in all of the elements. We can then use the reciprocity principle to reconstruct the potential differences at the electrodes for a source placed in any element (see Fig. 1).

The construction proceeds as follows: first, we choose one electrode as ground (i.e., we will force its potential to be zero). For each of the other M electrodes, one at a time, we place a current source, I, perpendicular to the surface at that electrode and a unit current sink at the ground electrode. The forward solution is then computed, resulting in a potential field, ϕ, defined at each node in the domain. We take the gradient of this potential field, yielding the electric field, $\mathbf{E}$, at each element in the head. A row of the lead field $\mathbf{L}_{\mathbf{e}}$ is computed by evaluating $(\mathbf{E}/-I)$ in every element. This process is repeated for each of the M source electrodes, producing the $\mathbf{L}_{\mathbf{e}}$ matrix (Fig. 2) satisfying

$$\mathbf{L}_{\mathbf{e}}\mathbf{s}_{\mathbf{e}} = \phi_r. \qquad (5)$$

Node Basis

The method for deriving the element-oriented lead-field constructs an $\mathbf{L}_{\mathbf{e}}$ basis that maps dipole components placed at the elements to potentials at the scalp-recording electrodes. One can also think of an alternative formulation based on the divergence of the source current density vector at each node, rather than three orthogonal current dipoles within each element. This lead-field formulation, which we refer to as *node oriented*, is depicted in Fig. 3. Our node-oriented basis is derived directly from the finite element stiffness matrix, $\mathbf{A}$, and right-hand side vector, $\mathbf{s}_{\mathbf{n}}$.

It is straightforward to solve the well-conditioned system (3):

$$\phi = \mathbf{A}^{-1}\mathbf{s}_{\mathbf{n}} \qquad (6)$$

to recover the potentials, ϕ, throughout the volume when the sources are known. For source imaging, however, we are interested not in the potentials everywhere in the volume, but only in the potentials at those few nodes corresponding to scalp electrodes recording sites. We introduce a matrix $\mathbf{R}$ that selects just the electrode potentials from ϕ. $\mathbf{R}$ is a $[K \times M]$ matrix (number of nodes by one less than the number of recording electrodes). Each row of $\mathbf{R}$ contains a single nonzero entry: the value 1.0 located at the column corresponding to the node index for that electrode.
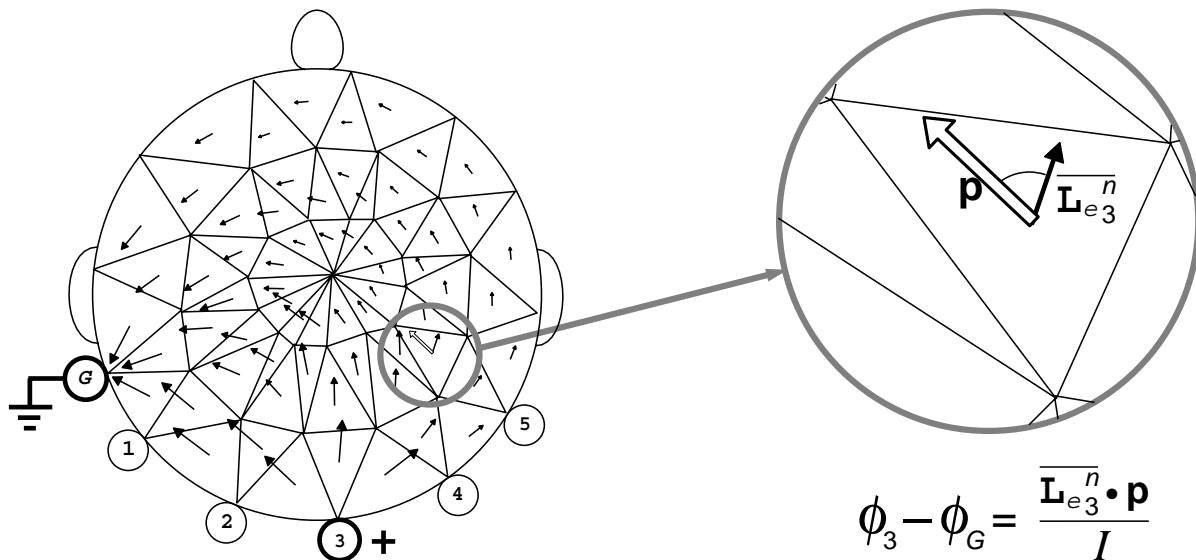
$$\phi_3 - \phi_G = \frac{\overline{\mathbf{L}_{e3}^{n}} \bullet \mathbf{p}}{I}$$

Figure 1: Depiction of the reciprocity-based method. A unit current is applied between electrodes "3" and "G". The reciprocity principle states that the voltage difference between "3" and "G" due to a dipole source $\mathbf{p}$ placed in element e^n will be equal to the dot product of $\mathbf{p}$ and the electric field in e^n.
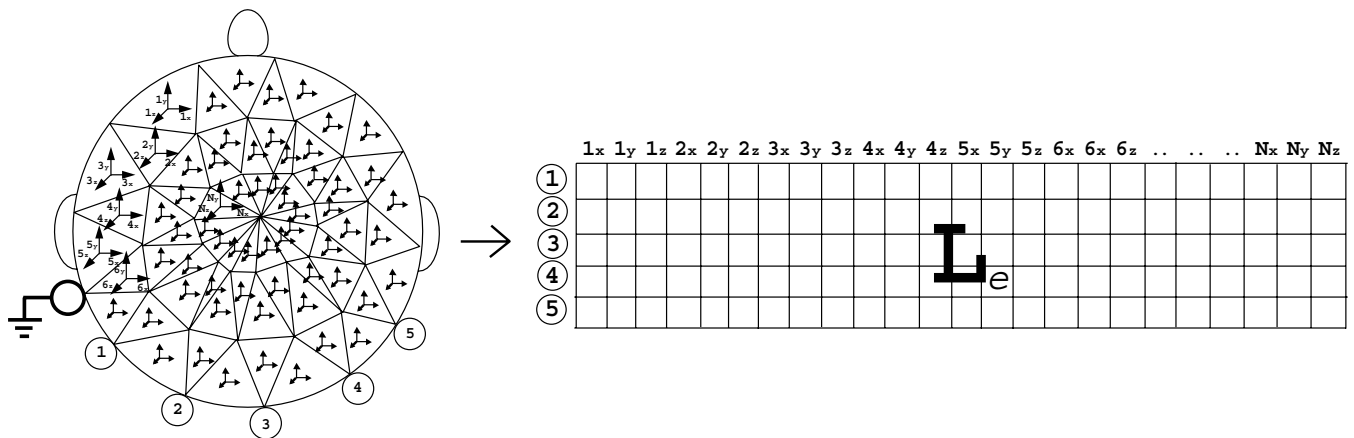

Figure 2: Depiction of the element-oriented lead-field basis. Each orthogonal dipole in each element corresponds to a column of $\mathbf{L}$, and each electrode corresponds to a row of $\mathbf{L}$. That is, each entry of $\mathbf{L}$ corresponds to the potential measured at a particular electrode due to a particular source.

From (6), we now select a subset of ϕ by applying $\mathbf{R}$:

$$\phi_r = \mathbf{R}\phi = \mathbf{R}\mathbf{A}^{-1}\mathbf{s_n} \qquad (7)$$

The $\mathbf{R}\mathbf{A}^{-1}$ operator is a node-oriented lead-field basis, which we term $\mathbf{L_n}$, and for which it follows that:

$$\mathbf{L_n}\mathbf{s_n} = \phi_r \qquad (8)$$

To efficiently compute $\mathbf{R}\mathbf{A}^{-1}$, we can exploit the sparse nature of $\mathbf{R}$. Since $\mathbf{R}$ contains only M nonzero entries, we need to construct only the corresponding M columns of $\mathbf{A}^{-1}$. This is accomplished by solving the equation:

$$\mathbf{A}(\mathbf{A}^{-1})_m = \mathbf{I}_m \qquad (9)$$

where $(\mathbf{A}^{-1})_m$ is unknown for source m. As with the construction of the $\mathbf{L_e}$ basis, this technique requires generating M forward solutions.

Lead-field comparison: $\mathbf{L_e}$ vs $\mathbf{L_n}$

The two lead-fields, element-oriented (5) and node-oriented (8), differ in several relevant ways.

The $\mathbf{L_e}$ formulation is based on having a dipole moment of a particular strength and orientation in each element. Because of this, $\mathbf{L_e}$ is most useful for reconstructing discrete dipolar sources. This is an appropriate method for localizing very focal neural activity, such as epileptic seizures or specific motor control tasks.

In contrast, the node-oriented $\mathbf{L_n}$ lead field is defined with values at the nodes. This means $\mathbf{L_n}$ will work best for recovering less focal, more distributed-type sources which are characterized by coordinated activity occuring at multiple neural locations. Such a solution should be well-suited to capturing diffuse cognitive events, such as language processing or the performance of complex tasks.

The size of the $\mathbf{L_e}$ basis is $[M \times (N \times 3)]$ (one less than the number of recording electrodes by three times the number of elements). There are often as many as a million elements in a finite element mesh, whereas there are typically only $M = 64$ or 128 recording electrodes. When using this lead-field basis for source imaging (i.e., solving $\mathbf{L_e}\mathbf{s_e} = \phi_r$ for a particular set of electrode recordings), it is clear that the solution will be grossly underdetermined.

The node-oriented basis, $\mathbf{L_n}$, is somewhat smaller: $[M \times K]$ (one less than the number of recording sites by the number of nodes). While there are still typically many more nodes (often as many as a hundred thousand) than electrodes, the system $\mathbf{L_n}\mathbf{s_n} = \phi_r$ is less under-determined than the element-based formulation. A typical unstructured finite element mesh contains six times as many elements as nodes, and the $\mathbf{L_e}$ basis requires three sources per element. This means the $\mathbf{L_n}$ basis will have about 6% as many degrees of freedom and a 94% smaller null-space. For example, the mesh used in our simulations contained 320,000 elements and 60,000 nodes. $\mathbf{L_n}$ had dimensions $(64 \times 960,000)$, and thus a null space of rank 959,936. In comparison, $\mathbf{L_n}$ had dimensions $(64 \times 60,000)$, and therefore a null space of rank 59,936. The smaller null space of $\mathbf{L_n}$ was a significant advantage when performing regularization.

Numerical Simulations

We constructed a realistic finite element head model from a volume magnetic resonance imaging (MRI) scan. The MRI data was segmented at the Brigham and Women's hospital,[20]

and a mesh was constructed using Krysl's variational Delaunay algorithm.[9] The full mesh contained 320,000 elements and 60,000 nodes. From this model, we selected 64 electrode recording sites at appropriate scalp surface nodes. (We note that if the true electrode locations do not correspond precisely to nodes in the mesh, the bases can still be constructed. The construction of $\mathbf{L_e}$ does not change at all, and the construction of $\mathbf{L_n}$ is only slightly modified. $\mathbf{R}$ can now have three nonzero entries per row, the electrode's barycentric weightings for the nodes of the scalp triangle containing it, rather than a single nonzero entry. This modification does not affect the efficiency of the construction.)

We then built $\mathbf{L_e}$ using the reciprocity method described. For each electrode current source, we solved a forward simulation in order to compute the electric field at each element in our model, and we stored that as a row of $\mathbf{L_e}$. Each solution required on average 8 s of wall-clock time using 8 SGI MIPS R10000 processors, resulting in a total of 9 min to compute all of $\mathbf{L_e}$.

Next, we computed $\mathbf{L_n}$, the node-oriented basis, by iteratively solving for $\mathbf{R}\mathbf{A}^{-1}$ one row at a time. Each row required approximately 7 s of wall-clock time, totaling 8 min to construct $\mathbf{L_n}$.

We then simulated a focal temporal seizure by placing a dipole source in that region of our finite element model and running a forward simulation. We stored the resulting electrode potential as ϕ. To validate our bases, we then recovered the position, orientation, and magnitude of the temporal source using the source localization algorithm described later.

Applications

One of the simplest applications of the $\mathbf{L_e}$ operator is to construct a single dipole *misfit field*. The misfit field is constructed as follows: position a dipole in an element; find the optimal magnitude and orientation for the dipole in that element using linear least squares optimization (all locations within the same element are equivalent); compute the two-norm misfit between the forward solution $\hat{\phi}$ due to that dipole, and the "measured" data, ϕ. Repeating these steps for all the elements in the model, we construct the misfit field

$$C_n = \|\phi - \hat{\phi}\| = \|\phi - \bar{p}_x \mathbf{L_e^{n,z}} - \bar{p}_y \mathbf{L_e^{n,y}} - \bar{p}_z \mathbf{L_e^{n,z}}\|. \qquad (10)$$

Clearly, the minimum of this field corresponds to the optimal dipole position for a single dipole model. Finding this minimum can be accomplished, for example, via an exhaustive search. We note that while the earlier description is for the $\mathbf{L_e}$ basis, a similar misfit function can be evaluated for the $\mathbf{L_n}$ basis.

Using the SCIRun problem solving environment,[16] we created the $\mathbf{L_e}$ matrix and constructed the misfit field for an occipital dipole source. A visualization of this field is shown in Fig. 4. The field values have been color-mapped onto a cutting plane positioned axially just below the source. Red triangles correspond to elements for which the contained optimal dipole produced a good fit to the measured data; in contrast, elements colored blue indicate regions for which even an optimally oriented dipole results in a poor fit to the measurements. Note the increase in the misfit for elements farther and farther away from the source, as well as the sharp discontinuities in and around the skull elements due to the large conductivity difference between bone and the surrounding tissue.
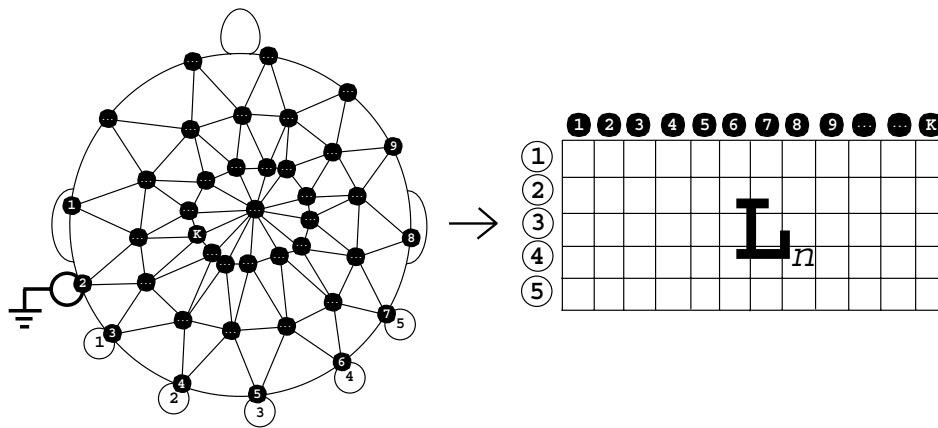
Figure 3: Depiction of the node-oriented lead-field basis. In contrast to Fig. 2, where the matrix columns corresponded to orthogonal dipoles, the columns now correspond to nodes. The node-oriented basis has approximately 94% fewer columns than the element-oriented basis and is better suited to recovering distributed source configurations.
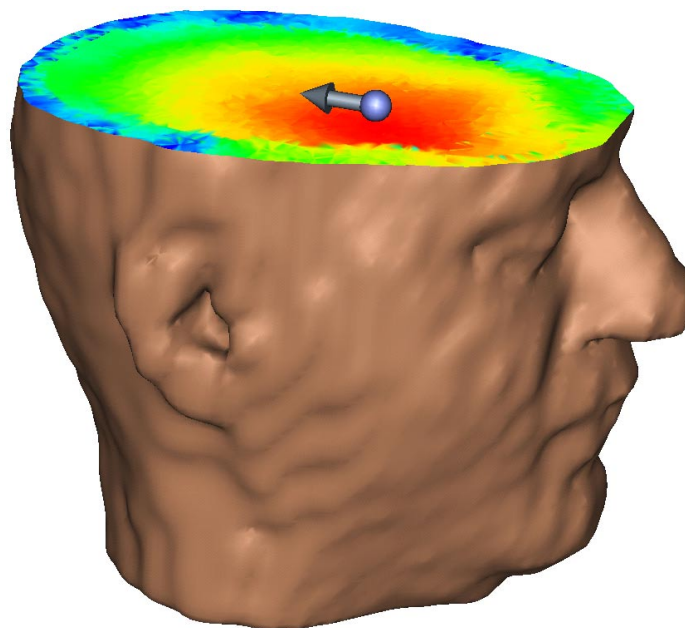

Figure 4: Visualization of the single dipole misfit field. The misfit between the "measured" data (due to the depicted dipole source) and the forward solution due to the optimal source for each element has been color mapped to an axial cutting plane. Blue values correspond to a large misfit, whereas red values correspond to a very small misfit.

Though computing the misfit function for a single element requires only a matrix-vector multiplication and a 3×3 system solve, for large models (e.g., with over 100,000 elements), the total time to build the field can reach up to an hour. If our goal is not to compute this field everywhere in the volume, but just to perform a *source localization* (recover an optimal dipolar source), we can be more efficient with our computation. Rather than evaluate the misfit function in all of the elements of the field, we can use an optimization technique to search for the minimal misfit. We note, though, that simple optimization techniques do not guarantee convergence to the global minimum. Gradient descent and Newton type methods are inapplicable in our case, since they use derivatives and the misfit field is only C_1 continuous. One of the search techniques which can be used in such a situation is downhill simplex.[15] In a three-parameter space, the simplex is a tetrahedron with four vertices which can "roll down" the misfit field and thus requires evaluation of the misfit function only at the locations along its path. A more detailed discussion of this method and its application to source localization in real head geometries can be found in Ref [22]. The major drawback of the downhill simplex is that it can get stuck in local minima and therefore requires multiple restarts.

An alternative optimization technique that can guarantee convergence to the global minimum of the misfit function is simulated annealing.[11] Simulated annealing is a stochastic simulation (Monte Carlo) method for global optimization that proceeds towards its solution by evaluating random samples in the parameter space. A downhill sample (that is, a sample at a location with a lower misfit), is always accepted as a new position. Additionally, an uphill sample is sometimes accepted as well, with a probability inversely proportional to the size of the increase in the misfit due to that step. As the algorithm proceeds, the probability of accepting uphill steps is decreased according to the cooling schedule - it is reduced by certain amount every several iterations. This can be summarized in the equation for the step acceptance (annealing equation)

$$Prob = \begin{cases} 1, & \Delta C < 0 \\ exp(-\Delta C/T), & \Delta C > 0 \end{cases} \qquad (11)$$

Thus, the implementation of simulated annealing requires the evaluation of multiple forward solutions (for our data, thousands) and until now it was only possible to use this method for source localization in spherical head models.[2, 8] However, with precomputed lead fields, we can now use simulated annealing for realistic head geometries. For our simulations, we randomly generate elements within a fix-sized neighborhood that generally contains only a small number of elements. We proceed by iteratively generating, evaluating and (in the case of step acceptance) stepping to the new best point. The cooling schedule we employ reduces the temperature by 10% after every ten iterations.

Using the simulated annealing source localization algorithm described earlier, we were able to successfully localize the source shown in Fig. 5. This localization was repeated from nine different starting locations. The algorithm successfully localized the source every time, requiring on average 5 min and 560 iterations to converge. In Fig. 5, we see a train of the most recent accepted steps indicated with gray arrows, the presently evaluated step depicted with the green sphere, and the true solution source shown as a red arrow. At the bottom, we have depicted the misfit of the current accepted step over each iteration. We note that the uphill steps are much more frequent during early iterations, and
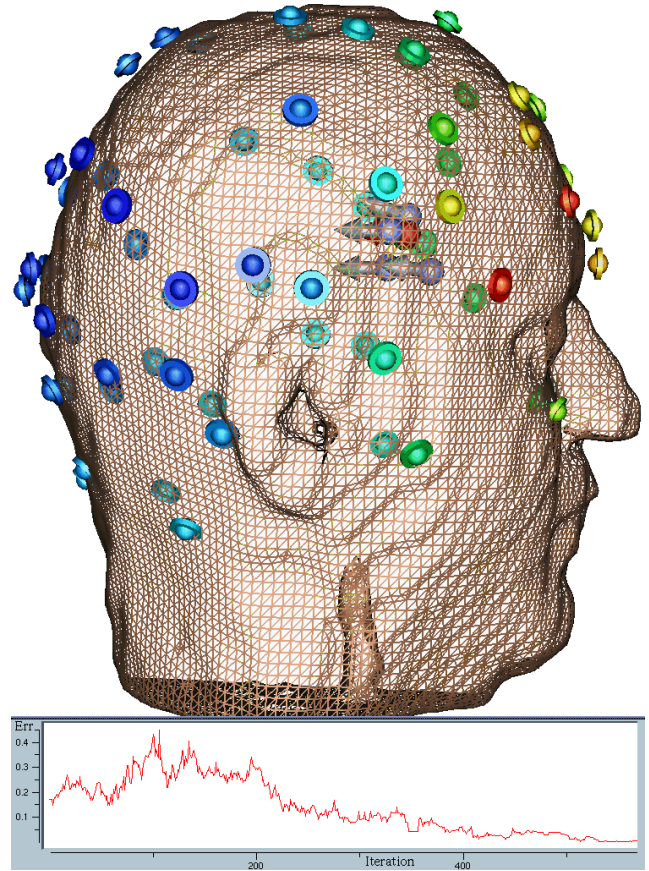

Figure 5: Visualization of the simulated annealing algorithm converging to a dipole source. The cluster of recently accepted steps is indicated by the gray vectors, while the true source is indicated in red. Two surface potentials have been mapped to each electrode. The disks represent the potentials due to the true source and the sphere inside of each disk represents the potential due to the latest evaluated search position. At the bottom, we show the currently accepted misfit through all iterations.

they taper off as the temperature cools over time.

In conclusion, we have proposed two methods for computing lead fields in finite element modeling of the head, and demonstrated the application of the lead field to source localization using simulated annealing. We believe the lead field can be successfully used in distributed source imaging, and plan to pursue such studies in the near future.

Acknowledgments

References

[1] H.C. Burger and J.B. van Milaan. Heart-vector and leads. Part I-*Br. Heart J.*, 8:157–61, 1946, Part II-*Br. Heart J.*, 9:154–60, 1947, Part III-*Br. Heart J.*, 10:229–33, 1948.

[2] J. Gerson, V.A. Cardenas, and G. Fein. Equivalent dipole parameter estimation using simulated annealing. *Electroencephalogr. Clin. Neurophysiol.*, 1994.

[3] I.F. Gorodnitsky, J.S. George, and B.D. Rao. Neuromagnetic source imaging with FOCUSS: a recursive weighted minimum norm algorithm. *Electroencephalogr. Clin. Neurophysiol.*, 95:231–251, 1995.

[4] H. Helmholtz. Uber einige gesetz der vertheilung elektrischer strome in korperlichen leitern, mit anwendung auf die thierischelektrischen versuche. *Ann. Phys. Chem.*, 29:211–233 and 353–377, 1853.

[5] J. Jin. *The Finite Element Method in Electromagnetics.* Wiley, New York, 1993.

[6] C.R. Johnson. Numerical methods for bioelectric field problems. In J.D. Bronzino, editor, *The Biomedical Engineering Handbook*, pages 162–180. CRC Press, Boca Ratan, 1995.

[7] C.R. Johnson. Computational and numerical methods for bioelectric field problems. *Crit. Rev. Biomed. Eng.*, 25(1):1–81, 1997.

[8] D. Khosla, M. Singh, and M. Don. Spatio-temporal EEG source localization using simulated annealing. *IEEE Trans. Biomed. Eng.*, 44(11):1075–1091, 1997.

[9] P. Krysl and M. Oritz. Variational delaunay approach to the generation of tetrahedral finite element meshes. *Int. J. Numer. Methods Eng.*, (in press).

[10] R. McFee and F.D. Johnston. Electrocardiographic leads. I-*Circulation*, 8:554–68, 1953, II-*Circulation*, 9:255–66, 1954, III-*Circulation*, 9:868–80, 1954.

[11] N. Metropolis, A. Rosenbluth, R. Rosenbluth, A. Teller, and E. Teller. Equation of state calculations by fast computing machines. *J. Chem. Phys.*, 21:1087–1092, 1953.

[12] C.E. Miller and C.S. Henriquez. Finite element analysis of bioelectric phenomena. *Crit. Rev. Biomed. Eng.*, 18:181–205, 1990.

[13] J.C. Mosher, R.M. Leahy, and P.S. Lewis. EEG and MEG: Forward solutions for inverse methods. *IEEE Trans. Biomed. Eng.*, 46(3):245–259, 1999.

[14] J.C Mosher, P.S. Lewis, and R.M. Leahy. Multiple dipole modeling and localization from spatio-temporal MEG data. *IEEE Trans. Biomed. Eng.*, 39(6):541–557, 1992.

[15] J.A. Nedler and R. Mead. A simplex method for function minimization. *Comput. J. (UK)*, 7:308–313, 1965.

[16] S.G. Parker, D.M. Weinstein, and C.R. Johnson. The SCIRun computational steering software system. In E. Arge, A.M. Bruaset, and H.P. Langtangen, editors, *Modern Software Tools in Scientific Computing*, pages 1–40. Birkhäuser Press, Boston, 1997.

[17] R.D. Pasqual-Marqui, C.M. Michel, and D. Lehmann. Low resolution electromagnetic tomography: A new method for localizing electrical activity in the brain. *Int. J. of Psychophysiol.*, 18:49–65, 1994.

[18] R. Plonsey. Reciprocity applied to volume conductors and the ECG. *IEEE Trans. Bioed. Electron.*, 10(1):9–12, 1963.

[19] S. Rush and D.A. Driscoll. EEG electrode sensitivity—an application of reciprocity. *IEEE Trans. Biomed. Eng.*, 16:15–22, 1969.

[20] W.M. Wells, W.E.L. Grimson, R. Kikinis, and F.A. Jolesz. Statistical intensity correction and segmentation of MRI data. In *Visualization in Biomedical Computing*, pages 13–24, Bellingham, 1994. SPIE.

[21] Y. Yan, P.L. Nunez, and R.T. Hart. Finite-element model of the human head: scalp potentials due to dipole sources. *Med. Biol. Eng. Comput.*, 29:475–481, 1991.

[22] L. Zhukov, D. Weinstein, and C. Johnson. Independent component analysis for EEG source localization. *IEEE Eng. Med. Biol. Mag.*, 19(3):87–96, 2000.